Exploring the Feasibility of Ray Tracing SAR Simulation on Building Damage Assessment

Chia Yee Ho, Erick Mas, Bruno Adriano, *Senior Member, IEEE*, and Shunichi Koshimura

***Abstract*—Synthetic aperture radar (SAR) imagery is indispensable for acquiring a comprehensive, large-scale topographical perspective of the Earth's surface, facilitating the evaluation of diverse scenarios spanning various events. However, integrating SAR imagery with ground truth data poses a formidable challenge, primarily due to the complex interactions of electromagnetic radar waves with the intricate features of the surface, characterized by multiple scatterings. This study seeks to bridge these disparities between authentic SAR and simulated by applying ray tracing SAR simulations within a meticulously controlled environment. Our investigation into SAR simulation focuses on evaluating the accuracy, precision, and reliability of theoretical models in representing surface features. Through ray tracing SAR simulations, we aim to understand better the complex interactions of electromagnetic radar waves with surface features, ultimately advancing our ability to interpret SAR imagery in diverse scenarios. The research findings indicate a robust correlation between the physical parameters of the surface and the backscattering levels observed in SAR simulations, underscoring the critical dependence of simulation accuracy on the granularity of the 3-D models employed. Moreover, this study delves into the consistency of modeling approaches in accurately replicating the assessment of building damage in postdisaster contexts, providing insights into the potential enhancements in disaster management and response strategies. The implications of these findings not only advance the understanding of SAR simulation fidelity but also pave the way for significant improvements in the application of SAR technology for disaster assessment and environmental monitoring.**

***Index Terms*—Building damage detection, disaster resilience, synthetic aperture radar (SAR) simulation, similarity assessment, simulated SAR.**

I. Introduction

THE expeditious and precise assessment of building damage following disasters is of paramount importance for effective response and rehabilitation efforts. In this context, synthetic aperture radar (SAR) technology emerges as a pivotal tool, owing to its unparalleled capability to delineate surface features under a wide array of conditions, encompassing inclement weather and nocturnal environments. The utility of high-resolution SAR systems, exemplified by platforms, such as ICEYE, Capella Space, and TerraSAR-X, which operate at the X-band frequency (approximately 31 mm), is particularly pronounced in the domain of building damage assessment. The high spatial resolution characteristic of X-band SAR systems is indispensable for the meticulous identification and evaluation of damage to individual structures, as substantiated by the literature [1], [2]. In addition, the versatility of SAR sensors across varying wavelengths underscores their significance in a diverse spectrum of applications, including but not limited to flood monitoring [3], deforestation analysis [4], sea ice observation [5], forest mapping [6], and oil spill detection [7].

In the realm of disaster assessment, methodologies, such as change detection leveraging pre- and postdisaster SAR imagery [8], [9], [10], alterations in back-scattering intensities [11], and the analysis of damaged building layovers [12] have been employed to ascertain the extent of damage. Nevertheless, the efficacy of these methodologies is contingent upon the availability of SAR datasets and the spatial resolution of the imagery. High-resolution SAR imagery is critical for urban and infrastructure monitoring, enabling the detection of minor structural changes [13]. However, the acquisition of high-resolution SAR datasets is frequently hampered by issues of availability and financial cost [14]. Despite its inherent advantages, the interpretation of SAR imagery, particularly in the aftermath of disasters, is compounded by the presence of debris, structural damage, and varied surface textures, which contribute to speckle noise [15]. It is within this context that SAR simulation gains prominence as a crucial intermediary between theoretical insights and practical application, especially in disaster assessment scenarios.

SAR simulation represents a computational endeavor aimed at producing synthetic radar images that endeavor to mirror the attributes of authentic images captured by SAR systems [16]. This process entails detailed modeling of electromagnetic radar signal interactions with terrestrial objects, taking into account parameters, such as frequency, polarization, and surface characteristics. Despite the potential of SAR simulation as a tool of significant utility, its practical deployment is hindered by several challenges. These include the simplified reflection models inherent in SAR simulators and the modeling of surface parameters, which often fail to comprehensively capture the

Manuscript received 15 March 2024; revised 21 May 2024; accepted 18 June 2024. Date of publication 24 June 2024; date of current version 8 July 2024. This work was supported in part by the JSPS KAKENHI Grants-in-Aid for Scientific Research under Grant 21H05001, Grant 22K21372, and Grant 22H01741, and in part by the Ministry of Education, Culture, Sports, Science and Technology (MEXT), and Co-creation Center for Disaster Resilience, Tohoku University and JST SPRING, under Grant JPMJSP2114. *(Corresponding author: Shunichi Koshimura.)*

Chia Yee Ho is with the Department of Civil and Environmental Engineering, Tohoku University, Miyagi 980-8579, Japan (e-mail: ho.chia.yee.s7@dc.tohoku.ac.jp).

Erick Mas, Bruno Adriano, and Shunichi Koshimura are with the Disaster Geo-Informatics Lab, International Research Institute of Disaster Science (IRIDeS), Tohoku University, Sendai 980-8572, Japan (e-mail: mas@irides.tohoku.ac.jp; bruno.adriano@tohoku.ac.jp; koshimura@irides.tohoku.ac.jp).

Digital Object Identifier 10.1109/JSTARS.2024.3418412

complex interplay between radar signals and terrestrial objects. Such limitations manifest in a tangible disparity between simulated and authentic SAR imagery. Moreover, the level of detail (LOD) utilized in SAR simulations plays a critical role [17], [18]. Simulated SAR data may not replicate fine details or complex structures with the same fidelity as authentic data, further exacerbating these disparities [19].

While existing studies have broached the feasibility of SAR simulation, the present research endeavors to provide a holistic examination of these limitations [20], [21]. Our objective is to elucidate the discrepancies between simulated and authentic SAR data, particularly in the context of real-world scenarios, and to augment the practical utility of simulated SAR data in disaster damage assessment. We aim to investigate the factors that influence the congruence between synthetic and authentic SAR data, including combinations of surface parameters, the LOD, and performance assessments in various damaged building contexts.

The rest of this article is organized as follows. Section II delineates related works in the field. Section III describes the data employed in this study. Section IV expounds upon the methodologies adopted. Section V presents experiments related to surface parameters and the granularity of the 3-D model. Section VI is dedicated to the application of SAR simulation in disaster scenarios. Finally, Section VII concludes this article.

II. Related Work

A. Overview

The domain of building damage mapping via remote sensing imagery has garnered substantial attention, particularly the advantages leveraged through SAR compared to optical satellite imagery. The unique attributes of SAR, including its side-looking geometry, capability to operate under any weather conditions, and distinct scattering mechanisms, render it an invaluable resource for real-time and postevent analysis in disaster-stricken regions [22], [23], [24]. The efficacy of damage detection and mapping critically depends on the quality and availability of SAR datasets, with an emphasis on acquiring consistent pre- and postdisaster imagery—a prerequisite often hampered by logistical and technical constraints.

The granularity of damage assessment is significantly compromised when employing low-resolution SAR data, underlining the necessity for high-resolution datasets, particularly within the X-band frequency range, to discern and accurately assess building damage [25]. However, the procurement of such datasets is frequently challenged by the limited availability of advanced high-resolution SAR satellites and the inherent delays in data capture attributable to their orbital dynamics, alongside the scarcity of high-resolution data [26].

Amid these challenges, SAR simulation has emerged as a pivotal research avenue, offering a pathway to synthesize high-fidelity datasets. SAR simulators are broadly classified into image simulators, producing processed imagery, and raw signal simulators, offering unprocessed SAR signals. Tools, such as ray tracing-based SAR simulator model (RaySAR) [17], CohRaS [27], SARsim [28], and SARViz [29], exemplify the advancements in SAR simulation technology, finding applications in disaster assessment and damage detection [30], [31], [32].

This investigation seeks to advance the application of simulated SAR imagery to enhance machine learning-based damage mapping techniques. Despite the promising outlook of synthetic SAR data in addressing the data scarcity dilemma, the transition to practical application is impeded by the simplified reflection models and the simulation of surface interactions, which fall short of capturing the complex dynamics between radar signals and terrestrial objects [14], [33], [34].

While machine learning techniques like cGANs can generate synthetic SAR images, but SAR simulators offer more control over the physics of radar-surface interactions. This control leads to more realistic SAR images [22], [33], [35], [36], [37]

B. Three-Dimensional Modeling

Accurate 3-D modeling is crucial in SAR simulation, especially in urban environments [38], [39], [40], where detailed building models are indispensable. Detailed building models are commonly created through the photogrammetric analysis of aerial imagery or data obtained from airborne light detection and ranging (LiDAR) systems. Using a 2.5-D view-dependent representation, as described by [41], enables the generation of models featuring shaped roofs and vertical walls, resulting in a dense triangle mesh. Automated LiDAR-generated models do not contain explicit representation 3-D shaped and may fall short of computer-aided design models, usually containing inconsistencies and errors. For instance, Auer [42] work on the 3-D model of Berlin central station involved a photogrammetric approach followed by software postprocessing. While photogrammetric methods may lack the detail required for very high-resolution SAR, it is imperative to include features, such as windows, balconies, and other facade details in simulations to match real radar signals accurately. Despite the emphasis on the importance of 3-D modeling in numerous papers, a comprehensive qualitative measure for assessing model detail levels is yet to be established. Furthermore, rendering high-detail models in simulations demands extended processing time and increased memory resources, especially when managing intricate details.

Our study aims to identify feasible minimum detail-level requirements in SAR simulations. While generating a single high-detail model is straightforward, the challenge intensifies when simulating a comprehensive SAR scene. Authentic SAR systems face a resolution limit determined by their wavelength, constrained by diffraction. SAR struggles to distinguish objects smaller than half of their wavelength in reality. It is noteworthy that RaySAR, with an infinite resolution cell, might simulate facade details beyond what authentic SAR captures. Hence, defining the limit of high-detail 3-D models in SAR simulation becomes crucial.

C. Surface Parameter Challenges

While surface parameters are crucial for accurate signal modeling in SAR simulations, determining them precisely remains a challenge. Existing methods, such as the Fresnel reflection

model explored by [42], [43], provide a general approximation, but achieving optimal settings for reflection coefficients and signal absorption remains a challenging aspect. Surface parameters are crucial for both radar signal interaction and SAR image quality. Accurate specification of these parameters becomes paramount for signal precision. However, simulating diffuse reflection introduces challenges, primarily due to the Lambertian backscattering assumption [42]. This assumption offers a coarse approximation, making adjustments to reflection coefficients and signal absorption settings intricate. Despite these challenges, adhering to the geometric considerations outlined by [42] for both specular and diffuse reflections remains essential for enhancing the accuracy of radar signal simulations.

D. Disaster Application

In the domain of disaster applications, Yu and Takeuchi [44] conducted an in-depth analysis of SAR backscattered intensity characteristics, specifically interpreting SAR images of earthquake-damaged buildings. Their study employed a canonical target known as Sandia Laboratory Implementation of Cylinders (SLICY) and a collapsed building model for simulations, contributing to the understanding and estimation of building damage resulting from earthquake events. However, limitations of these simplified 3-D models hinder the capture of real-world details, especially in simulations of complex damage scenarios, such as earthquake-induced building collapses. Existing methods for simulating damaged buildings in SAR simulation suffer from two limitations. For example, the damaged state models generated through the WallStat program[1] fall short of accurately representing the damaged state of houses, potentially due to insufficient facade detail in low-polygon models or software optimization issues. In addition, the current simulation methods struggle to accurately depict these complex damage scenarios, such as those caused by earthquakes. Walls are often depicted as crumbling in entire sections, failing to capture the finer details of how individual pieces might move during a collapse.

Expanding the scope of SAR simulation applications in analyzing damaged buildings, the authors in [20], [31], and [32] conducted studies that employed the CohRas SAR simulator and TerraSAR-X postevent data. Kuny et al. [31] focused on examining signatures of various types of building damage for damage type classification. In [32], the emphasis shifted to differentiating SAR signatures of debris and high vegetation, while Kuny et al. [20] distinguished debris from patterns like vegetation and gravel in TerraSAR-X postevent data. Although these applications effectively address damaged indicators like debris, their reliance on generalized 3-D models, particularly for high-rise buildings, raises concerns about the lack of diversity in extracted damage signatures, potentially leading to inadequate results and false positives.

In contrast, our approach addresses this gap by incorporating various 3-D models, specifically tailored for residential buildings and aligned with the European Macroseismic Scale (EMS-98) damage classification. This comprehensive approach enables a thorough building damage assessment across categories from no damage to destruction. Beyond damage classification, our focus extends to distinguishing signatures between multiclass damage, enhancing the practicality of real-world applications. Theoretical simulations for EMS-98 buildings form the basis for discerning distinct signatures, laying a foundation for future reference.

[1]https://www.rish.kyoto-u.ac.jp/ nakagawa/

III. Data

This section provides an overview of the data utilized, including the study area, LiDAR data for creating the 3-D model, and SAR imagery. The subsequent details elaborate on each dataset's relevance and significance.

A. Region of Interest

The study areas encompass the Onagawa nuclear power plant situated in Onagawa, Oshika District, and Ishinomaki City, Miyagi Prefecture, Japan, depicted in Fig. 1. Notably, despite its proximity to the earthquake epicenter, the International Atomic Energy Agency inspection in 2012 reported remarkably undamaged structural elements of the nuclear power station [45]. This observation holds significance considering the magnitude of ground motion experienced during the earthquake [46].

The specific selection of the Onagawa nuclear power plant as our study area is deliberate and driven by distinct factors. This region is characterized by the availability of high-resolution SAR (spotlight mode) with a wavelength of 3.1 cm, aligning with our research objectives. Leveraging the highest resolution SAR facilitates the exploration of two pivotal aspects: 1) comprehending the disparities between simulated and authentic SAR, delving into the intricacies of surface parameter representation in the real world, and 2) establishing minimum requirements for the LOD of 3-D models in SAR simulation.

B. TerraSAR-X Data

The experiments conducted in this study utilize TerraSAR-X imagery in Spotlight mode data obtained from Miyagi Prefecture, as depicted in Fig. 1(b). The TerraSAR-X dataset serves as the ground truth for our comparative analysis. Ensuring precise imaging geometries in generating simulated SAR data is essential for accurate comparisons and assessments.

Imaging geometry in SAR refers to the specific geometric parameters and characteristics of the radar imaging process. These parameters encompass information, such as the sensor position, the scene center, and the incidence angle at which the radar beam intersects the surface. The accuracy and quality of the simulated SAR images directly hinge on these parameters.

The TerraSAR-X data, provided as an enhanced ellipsoid corrected product, undergoes several processing steps. Calibration is performed, incorporating a Geocoded incidence angle mask. In addition, a Lee speckle filter with a 7×7 window size is applied to reduce noise. The final image is transformed into a sigma-naught imagery, ranging from -35 to 5 dB.

To further categorize ground surfaces and buildings within the study area (Onagawa nuclear power plant), we conducted

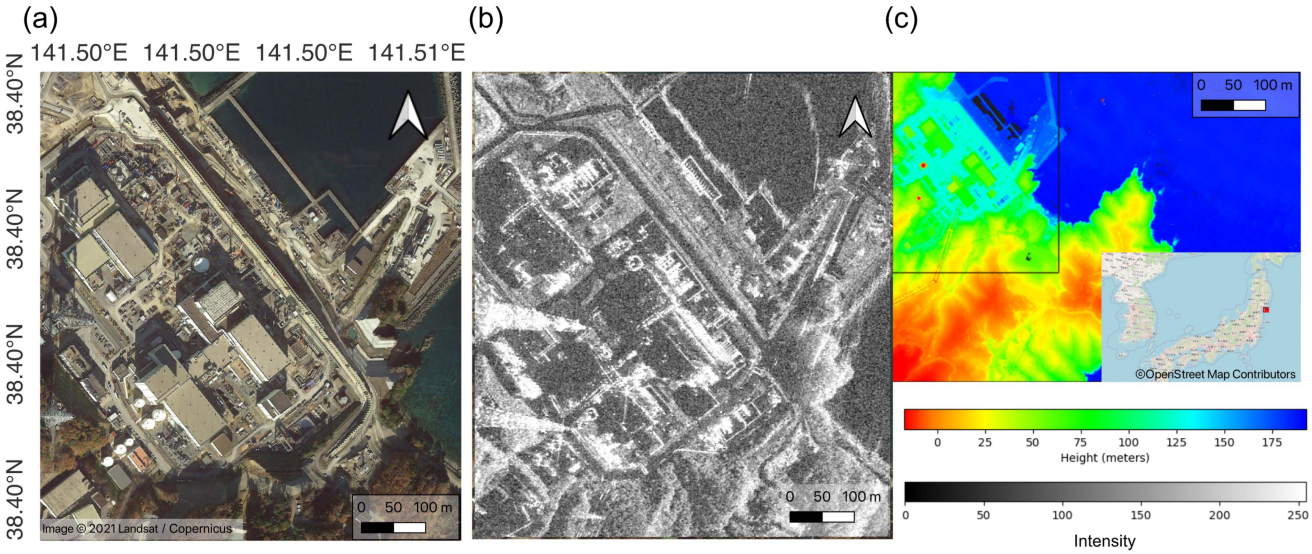

Fig. 1. Study area. (a) Optical Satellite Image capturing visual characteristics. (b) TerraSAR-X Image for SAR observations. (c) LiDAR view providing detailed topographical insights.

TABLE I
IMAGING GEOMETRIES OF THE TERRASAR-X SPOTLIGHT MODE

Parameters	Details
Acquisition date	August 19, 2011
Orbit direction	Descending
Looking direction	Right
Polarisation	HH (H: Horizontal)
Imaging mode	SpotLight mode (HS)
Incidence angle	47.95°
Azimuth resolution	1.15 (m)
Slant range resolution	0.588 (m)
Ground range resolution	1.00(m)

a classification into building and ground surface classes. The primary objective is to identify unique surface parameter combinations for each category, contributing to a comprehensive understanding of the features within the study area.

To accurately simulate the sensor orientation in a SAR scene, we estimated the sensor orientation between the scene center and the sensor position using TerraSAR-X parameters, including the sensor's X, Y, and Z positions, and the incidence angle. This approach ensures the precise simulation of the sensor orientation, facilitating the generation of SAR images that closely resemble authentic SAR data. Such accuracy is crucial for obtaining reliable results across various applications.

Table I presents the satellite specifications of TerraSAR-X used in our simulations.

C. LiDAR Data

The LiDAR point cloud, showcased in Fig. 1(c), features a pulse rate of 70 kHz, a scan rate of 38 Hz, and a density of 0.3 cm. The digital elevation model (DEM) with a ground sampling distance of 1 m is sourced from the Geospatial Information Authority of Japan (GSI). To facilitate compatibility and interoperability with different lidar processing tools, the LiDAR point cloud, initially presented in ASCII gridded XYZ coordinates, undergoes processing using environment for visualizing images (ENVI LiDAR). This processing step aims to convert the data into the widely adopted LAS format. For further details, refer to the Geospatial Information Authority of Japan's website.[2]

IV. METHODS

In this study, we employ a comprehensive methodology. Initially, LiDAR data undergo preprocessing to generate a DEM. Utilizing a modified DSM derived from LiDAR as input, we simulate SAR images using a RaySAR. Subsequently, we compare the simulated SAR images with authentic SAR data to assess any disparities.

In the subsequent phases, we explore the following three key aspects:

1) complexities of surface parameters;
2) minimum requirements of LOD;
3) SAR simulation for damaged buildings.

The framework is visually represented in Fig. 2.

A. RaySAR

RaySAR, a 3-D SAR simulator [17], utilized the open-source ray tracer POV-Ray to analyze signatures in azimuth, range, and elevation within the SAR imaging geometry. Tailored for urban environment simulations, RaySAR utilizes orthographic projection in azimuth and elevation for the SAR system, along with a signal source emitting parallel light. RaySAR can simulate an ideal SAR system with infinite resolution in azimuth, range, and elevation, allowing the separation of scatterers contributing signals to the same SAR image pixel in elevation. It takes a 3-D model and a contributions file as input, where the contributions file contains crucial details, including azimuth coordinates, range coordinates, intensity, bounce level, incidence angle, range geometry (slant range or ground range), and

[2]https://fgd.gsi.go.jp/download/ref_dem.html

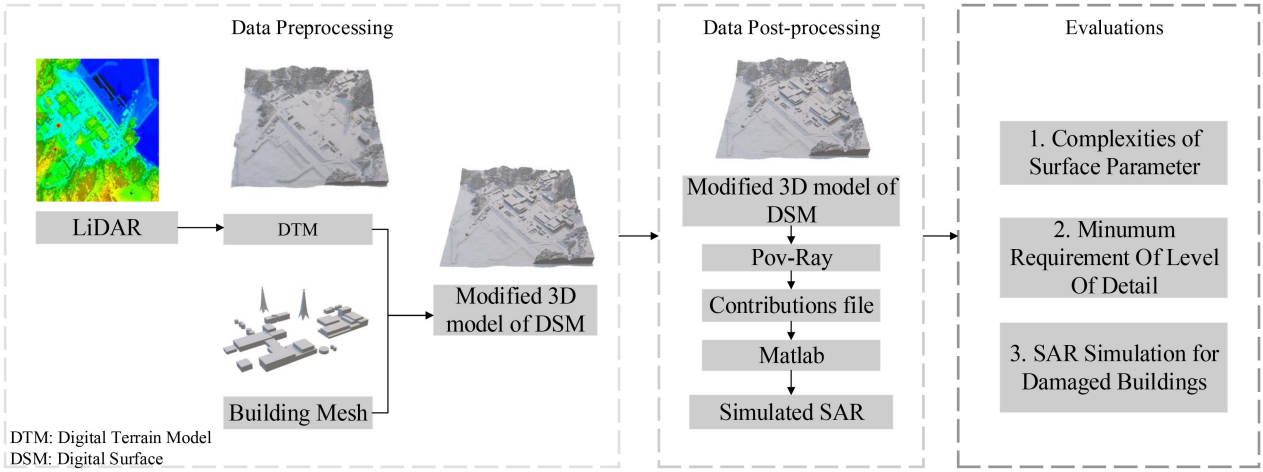

Fig. 2. Methodology overview—A graphical representation of the multistep methodology employed in this study.

angle. These parameters collectively contribute to the generation of simulated SAR images.

B. Surface Parameter Optimization

In SAR simulation, surface parameters are important for accurately capturing authentic SAR characteristics. These parameters, including correlation length, permittivity, and object geometry, influence the strength of radar signals backscattered to the SAR sensor. They define the characteristics of the modeled surface and govern radar wave interactions. However, the sensitivity of 3-D models to surface parameter choices is a crucial consideration. Simulated SAR images may potentially miss or underestimate signatures visible in authentic SAR data, presenting a worst-case scenario. A notable challenge lies in selecting appropriate coefficients for simulating urban objects. The following provides concise descriptions of each surface parameter.

1) *Reflection:* This parameter represents the amount of radar energy reflected by the surface. It determines the overall brightness or intensity of the SAR image pixel corresponding to the surface.
2) *Diffuse:* The diffuse coefficient describes the scattering behavior of the surface. It accounts for the random scattering of radar waves in different directions, contributing to the overall backscattered signal.
3) *Specular:* The specular coefficient represents the specular reflection of radar waves from a smooth surface. It accounts for radar energy's focused or directed reflection in a specific direction, creating bright spots or highlights in the SAR image.
4) *Roughness:* The roughness coefficient characterizes the surface roughness or texture. It accounts for the variations in height or irregularities on the surface, which affect the scattering behavior and intensity of the backscattered radar signal.

Fig. 3 illustrates how adjusting surface parameters such as reflection, diffuse, and specular influences the visual characteristics of the simulated SAR images. These visual distinctions

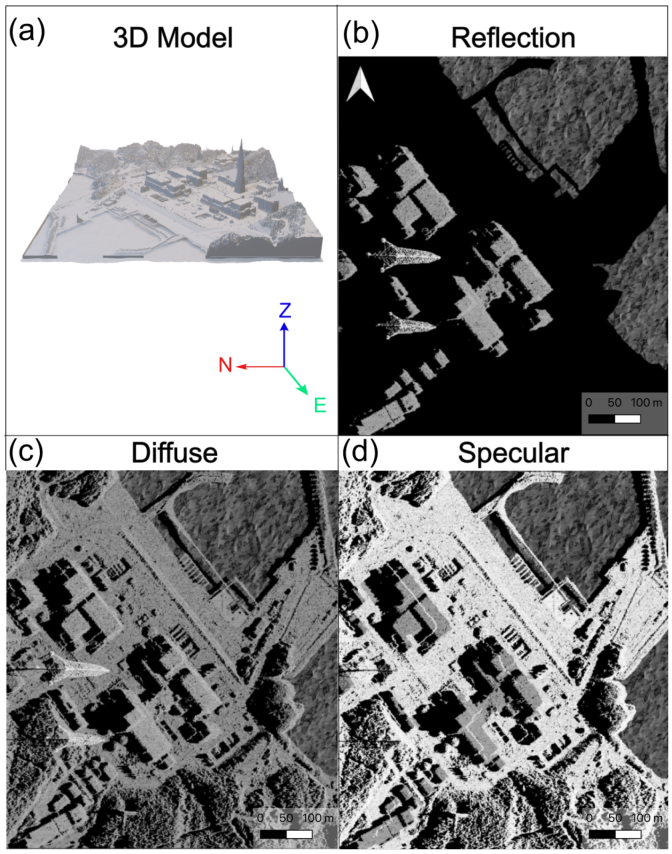

Fig. 3. Effect of varying surface parameters on simulated image appearance on ground surface only: R = Reflection, D = Diffuse, S = Specular. (a) 3-D model of Onagawa power plant. (b) Simulated image with only reflection components (R: 1.0, D: 0.0, S: 0.0). (c) Simulated image with only diffuse components (R: 0.0, D: 1.0, S: 0.0). (d) Simulated image with only specular components (R: 0.0, D: 0.0, S: 1.0). Heading angle = 188.94°, look angle = 68.68°.

in SAR imagery are essential for interpreting the influence of surface parameters. For example, (a) demonstrates the 3-D model used for SAR simulation, (b) demonstrates a total black image with reflection, diffuse, and specular values set to 0.0. In (c), changing only the diffuse value to 1.0 (maximum) results in

TABLE II
DEFINITION OF SURFACE PARAMETERS FOR ANGULAR-DEPENDENT DIFFUSE SIGNAL REFLECTION FROM BARE SOIL

Parameter	Low roughness	Medium roughness
Surface geometry		
Standard deviation	0.1 cm	0.4 cm
Correlation length	16.8 cm	8.4 cm
Specular coefficient (RaySAR)	0.7	0.5
Weight for specular reflection (RaySAR)	0.7	0.5
Roughness parameter (RaySAR)	8.5×10^{-4}	3.3×10^{-3}

a slightly brighter overall image. Meanwhile, (d) presents a very bright image by setting specular to 1.0, while the other values remain at 0.0.

The simulated image highlights the significant impact of surface parameters. The variations in reflection, diffuse, and specular properties, as well as roughness, showcase the influence of these parameters on the appearance of SAR imagery.

Table II, as summarized in [42], provides recommended settings for surface parameters in the RaySAR model. These settings, derived from bare soil examples relevant to radar signal interactions, include values for surface standard deviation, correlation length, and roughness factor.

Compared to the recommended settings from Table II, our approach takes an alternate direction by employing a systematic analysis to derive optimal surface parameters for radar signal interactions, notably without relying on explicit permittivity information. In contrast to methods explicitly considering permittivity, our approach emphasizes efficiency and simplicity. We comprehensively explore the parameter space through exhaustive comparisons across all possible surface parameter combinations, allowing for effective differentiation between building and ground surfaces. The experiment to evaluate suitable surface parameters is detailed in Section V-A.

C. Three-Dimensional Modeling

In SAR simulation, the quality of simulated SAR images relies on the precision of the 3-D modeling process, with the Onagawa nuclear power plant model (Fig. 3 (ai) serving as the foundation, accurately representing Earth's surface features, enabling detailed analysis of radar signal interactions and the generation of backscattered signals that closely resemble authentic SAR data. We used LiDAR point cloud data to construct the DSM, forming the basis for the 3-D model within the RaySAR framework. The complexity of a 3-D model is expressed in terms of vertices, faces, and triangles as quantitative measures of a 3-D model's intricacy and LOD. The different viewing angles of LOD models are shown in Fig. 4, and the complexity of each LOD is summarized in Table III.

1) *DSM model:* A digital surface model (DSM) is a top-down 2-D representation of a 3-D scene presented as an image, where each pixel encodes both geographical coordinates and the elevation at that specific point. In our method, we generate the DSM model using a point cloud derived directly from a 3-D scene processed with ENVI LiDAR. The resulting DSM comprehensively captures the heights of all surface features, including buildings, vegetation, and other structures. This DSM serves as the foundational element for our assessment, providing crucial elevation information for detailed comparisons.
2) *LOD1 model:* The emphasis is on conceptual modeling in its most primitive state. The building is portrayed with rough sizing and a basic layout. To achieve this, we utilized a model from the Sketchup 3-D Warehouse.[3] This LOD1 model provides a preliminary and rudimentary representation of the nuclear power plant.
3) *LOD2 model:* It represents an approximation of geometry. The model is crafted from scratch using Blender [47], with the scale ratio determined from orthographic photos obtained during the survey and aerial imagery from Google Image Satellite. This LOD encompasses both the traditional schematic design and preliminary high-level coordination.
4) *LOD3 model:* This model represents precise geometry, including specific elements, objects, or assemblies that are accurate in quantity, size, shape, location, and orientation. It encompasses all structural elements and basic architectural features, such as air conditioners, building frames, and bars. Utilizing blender, we built upon the LOD2 model to incorporate additional detailed facades. To ensure accuracy, high-resolution Google Earth images were used as references for proportions, and shadow lengths were analyzed for height estimation, validated against the DSM model. The facades were meticulously crafted with specific elements to enhance accuracy.

TABLE III
COMPLEXITY OF DIFFERENT LOD IN 3-D MODELS OF DSM, LOD1, LOD2, LOD3

LOD	Vertices	Faces	Edges
DSM	7266	13 916	21 192
LOD1	69	124	191
LOD2	1806	3317	5082
LOD3	110 518	214 418	325 142

D. Similarity Evaluation Metrics

To verify the similarity between authentic and simulated SAR, particularly for images with subtle feature differences, metrics, such as peak signal-to-noise ratio (PSNR) and the structural similarity index (SSIM) [48] are commonly applied. These are also used to quantify the quality of the image reconstruction

[3]https://embed-3dwarehouse.sketchup.com/model/ba6d15b469d01d3bc75d8a569ec40cc0Onagawa-Nuclear-Power-Plant

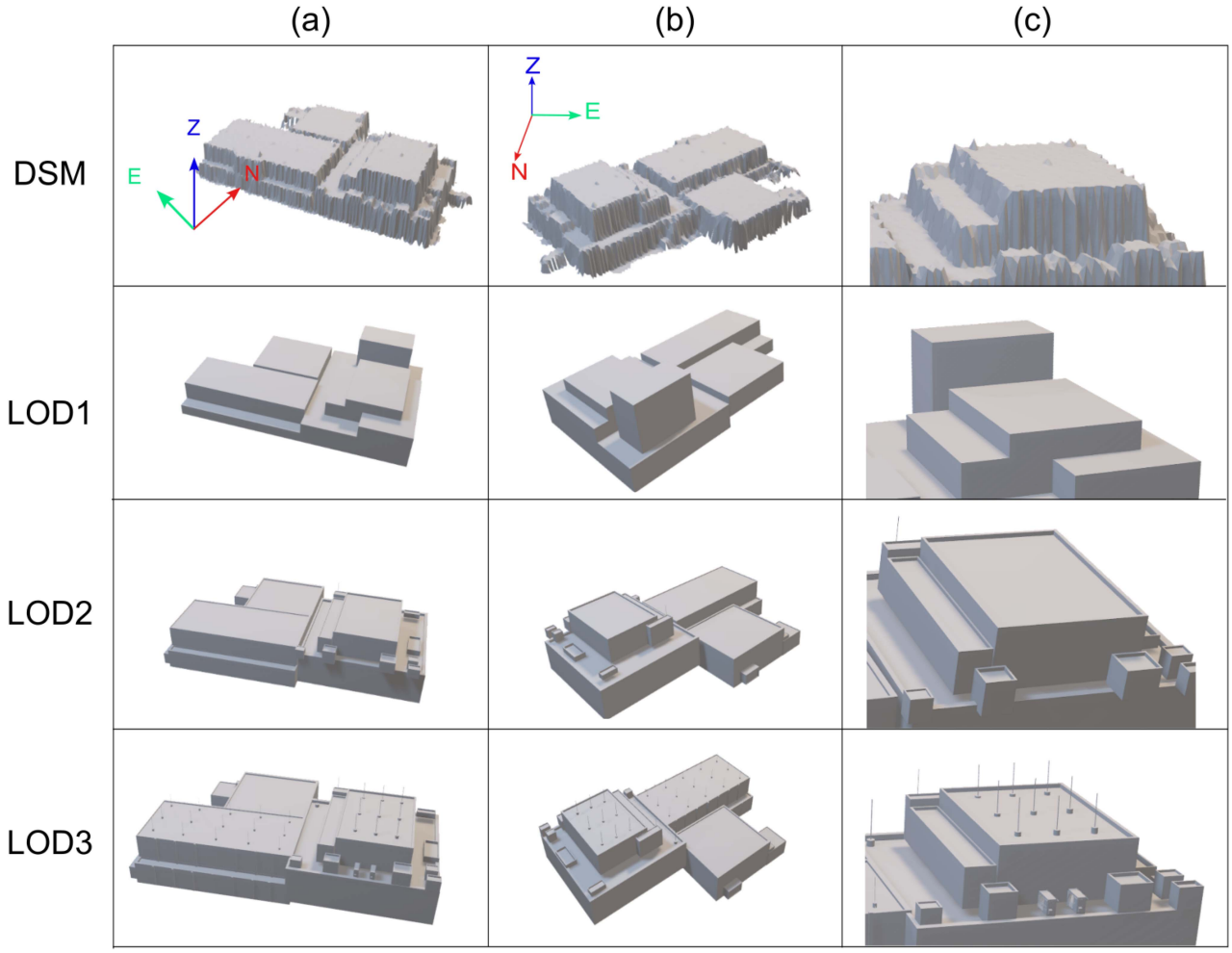

Fig. 4. Illustration of 3-D model of Onagawa nuclear power plant. (a) Front view. (b) Side view. (c) Zoomed-in view.

and lossy compression and are effective for evaluating broad structures.

1) Peak Signal-to-Noise Ratio: PSNR is a widely used metric for assessing the quality of reconstructed or simulated images compared to the original or reference images [49]. It quantifies the ratio of the maximum signal power to the power of the noise present in the image. Higher PSNR values indicate a stronger similarity between the simulated SAR images and the authentic SAR data.

The PSNR is calculated using the formula

$$\text{PSNR} = 10 \log_{10} \left(\frac{\text{MAX}^2}{\text{MSE}} \right) \tag{1}$$

where MAX is the maximum possible pixel value (usually 255 for 8-b images) and MSE is the mean squared error between the reconstructed or simulated image and the reference image.

2) Mean Squared Error: mean square error (MSE) measures the average squared difference between corresponding pixel values in two images (original and reconstructed). It is an absolute error metric that directly quantifies the magnitude of differences between pixel values. Lower MSE values indicate better similarity, with a value of 0 indicating perfect similarity

$$\text{MSE} = \frac{1}{N} \sum_{i=1}^{N} (I_i - \hat{I}_i)^2 \tag{2}$$

where MSE is the mean squared error, N is the number of pixels, I_i is the intensity of pixel i in the original image, and $\hat{I}_i$ is the intensity of pixel i in the reconstructed image.

3) Structural Similarity Index: The SSIM is a metric that evaluates the structural similarity between two images, considering aspects, such as luminance, contrast, and structural information [50]. SSIM is valuable for assessing the similarity between simulated and authentic SAR images, surpassing simple pixel-wise comparisons. By capturing relationships and patterns in the images, SSIM provides insights into how well simulated SAR images replicate the visual characteristics and overall structure of authentic SAR data [50].

The SSIM is calculated using the formula

$$\text{SSIM}(x, y) = \frac{(2\mu_x \mu_y + C_1)(2\sigma_{xy} + C_2)}{(\mu_x^2 + \mu_y^2 + C_1)(\sigma_x^2 + \sigma_y^2 + C_2)} \tag{3}$$

where x and y are the input images being compared, μ_x and μ_y are the means of x and y, respectively, σ_x and σ_y are the standard

deviations of x and y, respectively, σ_{xy} is the covariance between x and y, and C_1 and C_2 are small constants to prevent division by zero.

We utilized normalized scores in our image similarity analysis to derive similarity scores from the three metrics: PSNR, MSE, and SSIM. Each metric was normalized independently across the entire dataset. The summation score (SUM) in (7), derived from summation with equal weights from (1) to (3) to derive the normalized value of PSNR, MSE, and PSNR [see (4)–(6)] from each evaluation metric, is used to quantify overall image similarity. The correlation coefficient formula, often denoted as ρ, is given by (8)

$$\|\text{PSNR}\| = \frac{\text{PSNR} - \text{PSNR}_{\text{min}}}{\text{PSNR}_{\text{max}} - \text{PSNR}_{\text{min}}} \tag{4}$$

$$\|\text{MSE}\| = 1 - \frac{\text{MSE} - \text{MSE}_{\text{min}}}{\text{MSE}_{\text{max}} - \text{MSE}_{\text{min}}} \tag{5}$$

$$\|\text{SSIM}\| = \frac{\text{SSIM} + 1}{2} \tag{6}$$

$$\sigma = \|\text{MSE}\| + \|\text{PSNR}\| + \|\text{SSIM}\| \tag{7}$$

$$\rho = \frac{\text{cov}(\mathbf{X}, \mathbf{Y})}{\sigma_X \sigma_Y} \tag{8}$$

where $\mathbf{X}$ represents the pixel values of the authentic SAR image and $\mathbf{Y}$ represents the pixel values of the simulated image. The correlation coefficient (ρ) measures the strength and direction of a linear relationship between these two variables. In addition, $\text{cov}(\mathbf{X}, \mathbf{Y})$ denotes the covariance between the pixel values of the $\mathbf{X}$ and the $\mathbf{Y}$, while σ_X and σ_Y represent the standard deviations of the pixel values, respectively.

V. Experiments and Results

In this section, we explore several factors that influence the quality of simulated SAR images. Our focus areas include the following:

1) surface parameter combinations;
2) the necessity for detailed 3-D models in simulated SAR images;
3) evaluating SAR simulation performance in different damaged building scenarios.

We use PSNR, MSE, and SSIM to evaluate the similarity between authentic and simulated SAR images.

A. Similarity Evaluation

In our process of evaluating similarity in SAR simulation, we initiate the alignment of authentic SAR images with their simulated counterparts. This alignment is achieved through the employment of the affine transformation technique and ground control points within the quantum geographic information system software [51]. Initially, the evaluation focuses solely on PSNR [see (1)], a metric that sheds light on pixel-level differences, offering a straightforward measure of overall pixel intensity changes. PSNR serves as a foundational metric, quantifying the overall fidelity of images by assessing intensity variations between corresponding pixels.

Our systematic analysis explores the influence of surface parameters on simulated SAR imagery, generating images with diverse parameter combinations, including roughness, reflection, specular, and diffuse settings. Notably, lower roughness values, particularly those close to 0, consistently yield higher PSNR scores for both building and ground surfaces.

In the context of SAR simulation, roughness characterizes surface irregularities. However, the impact of roughness on pixel-level changes may be less significant compared to other surface parameters, such as reflection, diffuse, and specular settings. Systematic analysis reveals that variations in roughness values exert a relatively smaller influence on simulated images. Lower roughness values, approaching 0, may not result in substantial pixel-level changes.

To identify and understand the primary factors influencing simulated SAR imagery, we emphasize parameters with a more pronounced effect. Reflection, diffuse, and specular settings emerge as dominant factors in pixel-level changes, making them crucial for evaluation. Consequently, our further exploration concentrates on reflection, specular, and diffuse parameters, spanning from 0.0 to 1.0 in increments of 0.1, resulting in a possible combination of 11^3 (1331 images).

To enhance the evaluation process, we incorporate SSIM in equation, which considers changes in brightness, contrast, and structure. SSIM is deemed a more robust measure of image quality. In summary, while PSNR and MSE provide fundamental insights, the comprehensive evaluation includes SSIM, ensuring a balanced assessment of both technical accuracy and perceptual quality in simulated SAR imagery.

The SUM value, representing the SUM of the three evaluation metrics, is calculated for each possible image through systematic analysis. Fig. 5 visualizes the results in line plots for both ground surface and building, revealing distinct trends. These trends become evident when examining the median sum values across three surface parameters—reflection, diffuse, and specular.

The detailed observations are listed as follows.

1) *Reflection:* Both ground surfaces and buildings exhibit minimal variation, suggesting an insignificant impact of reflection.
2) *Diffuse:* Both buildings and ground surfaces demonstrate an ascending trend, indicating that higher specular contributions correspond to higher similarity scores.
3) *Specular:* Buildings and ground surfaces manifest a similar pattern to the diffuse surface parameter, where higher surface parameter values correspond.

In comparison to the suggested parameters detailed in Table II, our approach recognizes the inherent challenges in defining surface parameters based on object, roughness, and geometry. While our systematic method effectively distinguishes between building and ground surface scenarios, it is essential to acknowledge the absence of a clear guideline for consistent parameter selection, as proposed in the referenced method. The parameters we have chosen align with the targeted distinctions in surface characteristics, emphasizing the importance of considering context and validation against real-world observations for accurate simulation. Notably, our method does not explicitly incorporate considerations related to material properties.

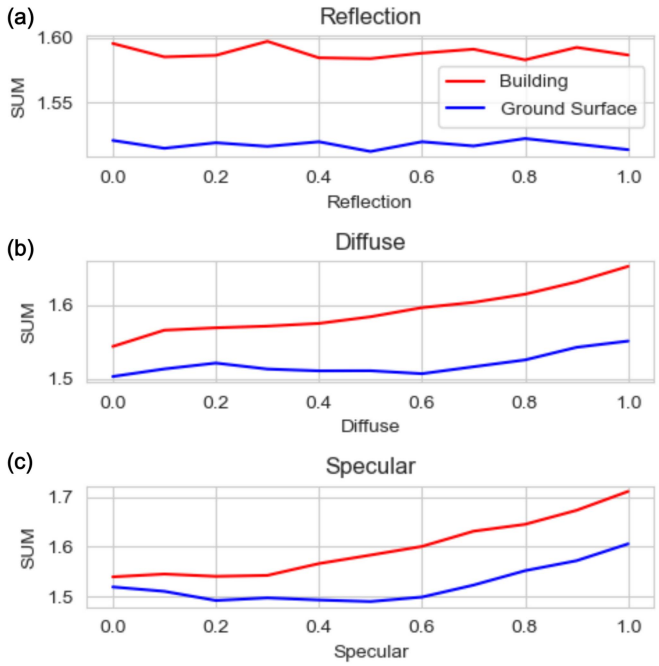

Fig. 5. Normalized median values of the SUM variable across various surface parameters. (a) Median normalized values of the surface parameter reflection. (b) Median normalized values of the surface parameter diffuse. (c) Median normalized values of the surface parameter specular.

TABLE IV
OPTIMIZED SURFACE PARAMETER COMBINATIONS FOR GROUND SURFACE AND BUILDING

Parameter	Object	
	Ground surface	Building
Reflection	0.8	0.3
Diffuse	1.0	1.0
Specular	1.0	1.0

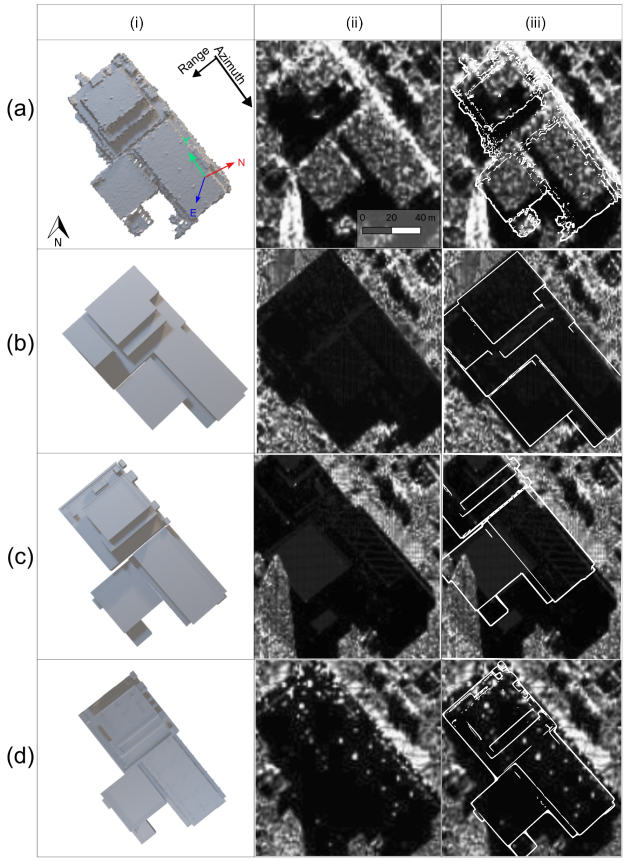

Fig. 6. Simulation results illustrating varied detail levels. (a) DSM model. (b) LOD1. (c) LOD2. (d) LOD3. Insets. (i) 3-D models, (ii) Simulated SAR image, (iii) Simulated SAR image overlayed with building edges.

B. *Influence of Detailed 3-D Model*

In SAR simulation, achieving accurate 3-D model representation is crucial, and different levels of detail (LODs) play a pivotal role in this process [52]. Our study investigates DSM, LOD1, LOD2, and LOD3, highlighting their significance in 3-D modeling. Integrating these LODs with surface parameters (see Table IV), Fig. 6 visually presents the simulated SAR imagery.

The findings illustrated in Fig. 6(ii) show distinct characteristics of each model. DSM (a)-(ii) demonstrates layover and backscattering, a result of the triangulated building structure. LOD1 (b)-(ii) depicts a pitch-black building without facade details. LOD2 (c)-(ii) shows slight shadowing but lacks intricate facade features. LOD3 (d)-(ii) shows high backscatter, especially from the antenna structure, along with a pronounced layover effect attributed to features like facades. Figs. 6(a)-(iii)–(d)-(iii) further emphasize the importance of overlaying building edges on simulated images for visual validation and verification of simulation results.

Our focus narrows to the green dot in the cross-sectional profile analysis (see Fig. 7), ranging from 40 to 100, providing insights into the primary building structure. The corresponding cross-correlation coefficients are presented in Fig. 7(a), where LOD3 stands out with the highest correlation value of 0.657 with the authentic SAR signal. In contrast, LOD1 exhibits the lowest correlation of 0.583, while DSM has a correlation value of 0.637, and LOD2 falls in between with a value of 0.612.

Fig. 7(b) focuses on a single row ($y = 40$) for a more detailed cross-sectional profile analysis, chosen for its inclusion of the building section and layover zone. In scenarios involving layover (indicated by the blue dot: C,D), DSM and LOD3 show slight correlations, suggesting closer matches between simulated and authentic SAR signals, possibly due to facades contributing to layover effects.

While LOD3 profiles demonstrate a noteworthy alignment with authentic SAR signals, particularly in building scenarios, the analysis suggests prioritizing LOD3 in SAR simulations to enhance fidelity and minimize mismatches. Importantly, considering practical factors, such as computational efficiency and time constraints, LOD3 proves to contain the minimum necessary facades—essentially capturing the essential building structure. This minimalistic representation, while falling short of perfection compared to the actual building with more facades, offers a practical compromise. The achievable similarity score with LOD3, coupled with its computational efficiency, makes it a viable choice for applications where a balance between accuracy and resource efficiency is crucial.

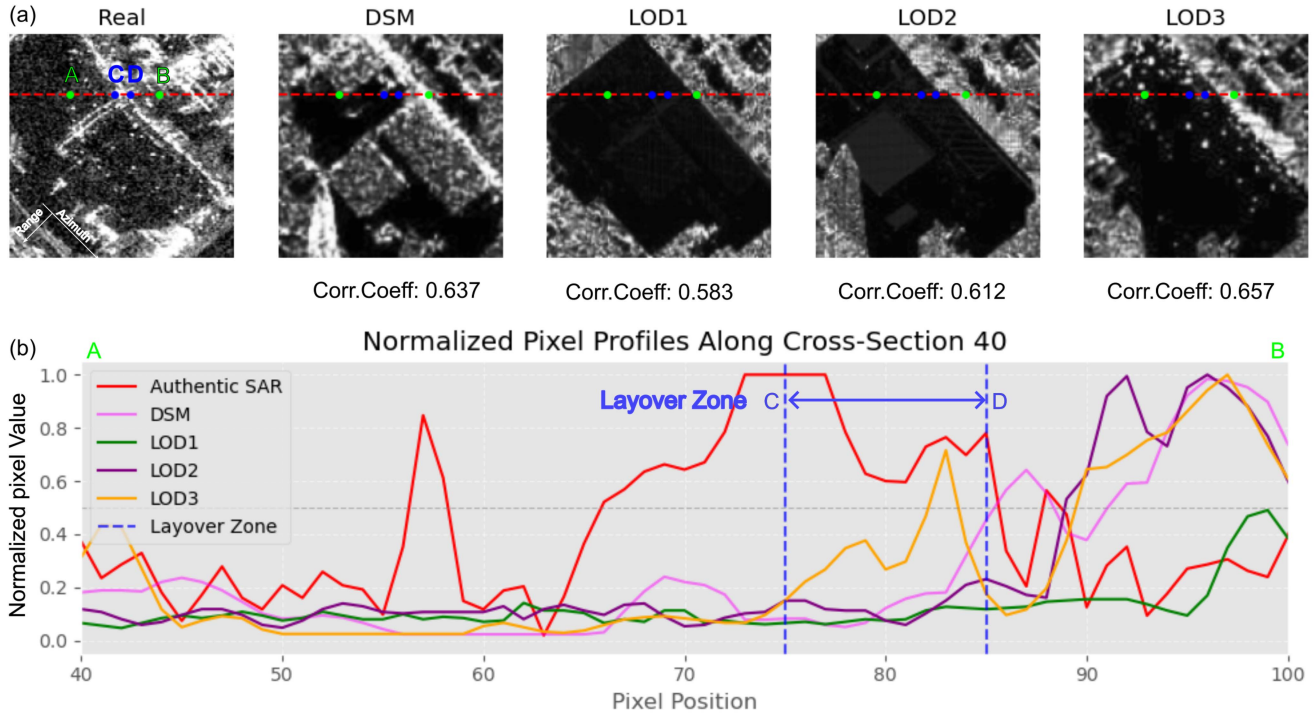

Fig. 7. (a) Simulated SAR scenes with different LODs, featuring layover zones (blue dot: C, D), cross-section lines (red lines), and main building (green dot: A, B). (b) Normalized pixel profiles along cross-section $y = 40$ in the full scene, including Authentic SAR, DSM, LOD1, LOD2, and LOD3. The red line denotes the cross-section line, and the blue line represents the corresponding layover zone.

VI. SAR Simulation for Damaged Buildings

SAR simulation presents distinct advantages over traditional optical satellite imagery when assessing damaged buildings. SAR imagery serves as supplementary data for interpreting building damage scenarios, relying on the backscattering phenomenon and layover extent. Unlike optical imagery, SAR images reveal persistent scattering patterns in intact buildings, while damaged structures exhibit alterations in backscattering or changes in layover extent, serving as detection indicators. To effectively utilize simulated SAR imagery for assessing damaged buildings in real-world scenarios, it is essential to discern the unique scattering patterns associated with intact and damaged structures. However, real-world SAR data is limited, with buildings often appearing small in SAR imagery, and high-resolution SAR imagery is scarce. Looking ahead, we plan to leverage pairs of SAR imagery captured before and after an event. By generating simulated SAR imagery for the pre-event scenario, we aim to evaluate its effectiveness in representing the pre-event condition for change detection in damaged buildings. Furthermore, we propose generating simulated SAR imagery based on 3-D models of damaged buildings to replicate unique backscattering features from various damaged structures. This approach involves training a model to recognize the distinct scattering properties of damaged indicators, such as components affected by damage on buildings.

This section offers a comprehensive overview of the suitability of SAR simulation in assessing damaged buildings, with a specific focus on EMS-98 buildings. We explore its effectiveness in capturing and analyzing the distinct features associated with damaged structures, particularly those outlined in the EMS-98 classification. In addition, the role of debris, another crucial marker of building damage, is examined to enhance our understanding of SAR's applicability in disaster assessment scenarios. Through this exploration, we aim to evaluate the valuable insights that SAR simulations can provide in the context of assessing and characterizing the impact on buildings subjected to various environmental and seismic conditions, including those affected by tsunamis and earthquakes, and specific categorical damages, such as structural failure and the collapse of the first-floor wall.

A. EMS-98 Damage Scale

We utilized the EMS-98 scale (accessible at[4]) to categorize building damage levels, ranging from negligible to destruction, as detailed in Table V. 3-D models representing different damage categories in typical Japanese residential households were generated, progressing from (a) to (e) based on building surveys.

Simulated SAR images were then generated from these 3-D models (see Fig. 8) at resolutions of 1.0 m Fig. 8(b) and 1.5 m Fig. 8(c). Minimal visible changes were observed at both resolutions for negligible or minor damage. For moderate damage, slight debris and structural deformations became apparent. In cases of heavy damage and destruction, even the lower resolution of 1.5 m revealed distinguishable extent and severity of

[4]https://www.gfz-potsdam.de/en/section/seismic-hazard-and-risk-dynamics/data-products-services/ems-98-european-macroseismic-scale

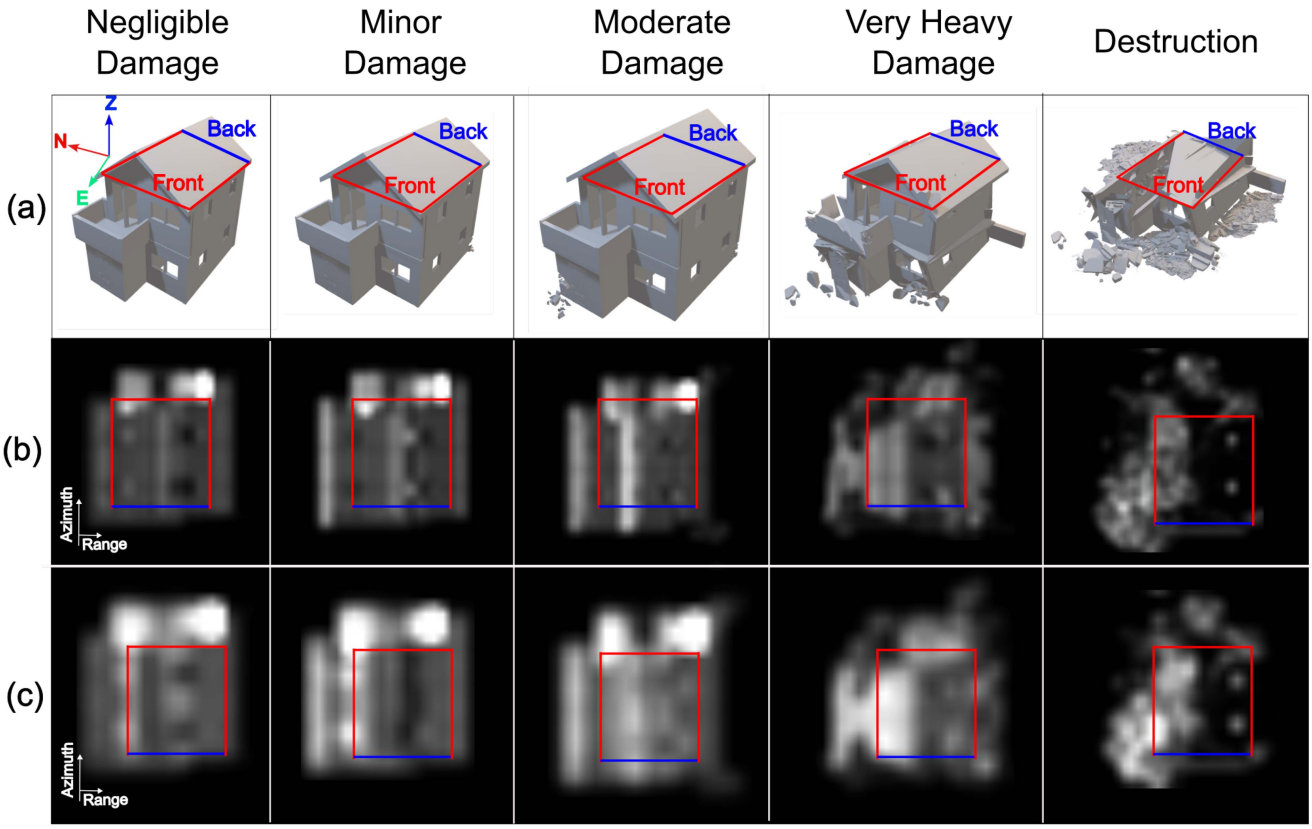

Fig. 8. Simulated SAR images illustrating varied detail levels of damage of EMS-98 buildings. (a) 3-D model representing different damage scenarios. (b) Simulation result at 1.0 m spatial resolution. (c) Simulation result at 1.5 m spatial resolution. The incidence angle is 37°, and the looking angle is defined by rotating the building while fixing the sensor position.

TABLE V
DESCRIPTIONS OF EMS-98 DAMAGED BUILDINGS

Severity	Descriptions
Negligible damage	Hair-line cracks in very few walls. Fall of small pieces of plaster only
Minor damage	Cracks in many walls; fall of large plaster pieces.
Moderate damage	Extensive cracks in most walls, Roof-tiles detached. Failure of individual nonstructural roofs and floods.
Very heavy damage	Heavy structural damage, serious failure of walls, partial structural failure of roof and floors.
Destruction	Very heavy structural damage; total or near collapse

damage. At 1.0 m resolution, building facades became more distinguishable.

In both resolutions, layover changes correlated with the degree of damage. Negligible, minor, and moderate damage showed no indications of destruction. However, severe damage and destruction exhibited distinct changes, especially in heavy damage, where debris crumbled and structural failure on the second floor was evident. The destruction class showed pronounced layover and shadow changes, reflecting substantial structural damage.

The findings indicate that SAR simulation effectively distinguishes between various damage classes at both low and high resolutions. Challenges in discerning the moderate damage class at low resolution suggest considerations for the feasibility of multiclass damage classification using SAR simulation. Further research and refinement of simulation techniques are essential to enhance the accuracy of multiclass damage classification.

B. *Earthquake and Tsunami Damage*

This section delves into the simulation of buildings affected by tsunamis and earthquakes, expanding beyond the focus of traditional damage assessment scales like EMS-98. The emphasis lies on capturing distinct characteristics, such as collapsed walls and roof damage, providing deeper insights into the nuanced impact of these disasters on urban structures. By incorporating these unique features into SAR simulation, the aim is to enhance the fidelity of the resulting images, thus validating the simulation's ability to represent the effects of tsunamis and earthquakes on buildings accurately.

Fig. 9(a)–(d) presents simulated images of these buildings from various looking angles (45°, 90°, 225°, 270°), showcasing the resolution set at 1.0 m. The exploration of SAR simulation's capability to generate images at different angles addresses potential limitations in capturing certain damages with real SAR sensors.

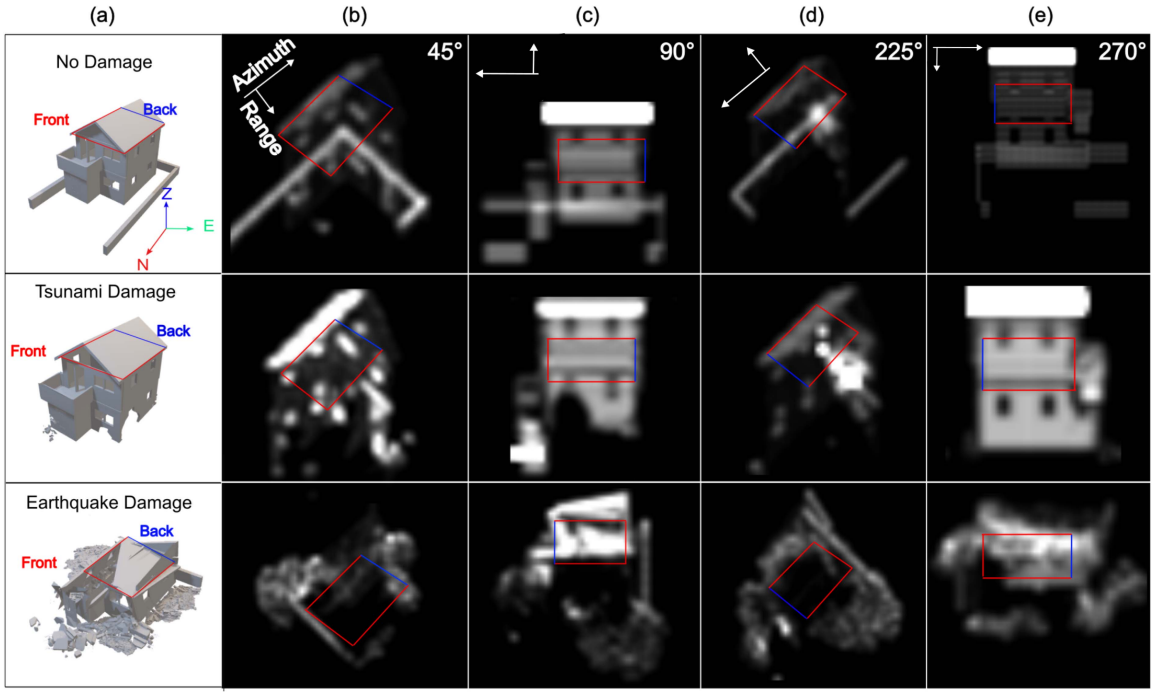

Fig. 9. SAR images generated at various angles. (a) 3-D models of varying damage levels. (b) 45° view. (c) 90° view. (d) 225° view. (e) 270° view. The incidence angle for these simulated images is 37°.

However, challenges persist in differentiating between buildings with no damage and minor damage in the simulated images. Possible reasons include the limited creation of debris or obscured damage from the side-looking geometry inherent in SAR simulation.

The insights from SAR simulations provide invaluable insights into the reflectance characteristics exhibited by debris and damaged components within earthquake and tsunami-affected structures. This enhanced understanding serves as a cornerstone for real-world SAR applications, facilitating more accurate recognition and assessment of the impacts induced by disasters on buildings.

The current results affirm the efficacy of SAR simulations in representing heavier damage categories within affected buildings. This assertion is supported by the observation that the diffuse component in SAR-simulated images is more pronounced than the specular component observed in undamaged structures. Consequently, we anticipate SAR simulations will significantly advance our capabilities in identifying and categorizing damaged building using real SAR data. Simulated SAR images offer valuable insights into the distinctive features of damaged structures. These images encapsulate unique characteristics that can be harnessed to train machine learning models, thereby augmenting the overall accuracy of damage assessment procedures. This includes the classification of observed damage into various categories, such as minor, moderate, or severe damage, tailored to specific types of disasters. By leveraging the rich information contained within simulated SAR imagery, machine learning algorithms can better differentiate and categorize different levels of damage, facilitating more precise and efficient damage assessment processes.

VII. Conclusion

This study comprehensively investigated the factors influencing the fidelity of SAR simulations. In previous discussions, factors contributing to realism in simulated SAR were not extensively discussed. Although some aspects, such as surface parameter settings and the influence of detail level in 3-D models, were briefly mentioned, a comprehensive analysis is still lacking. In addition, the suitability of SAR simulation for assessing building damage in disaster contexts has not been fully explored. This research aims to address these gaps.

To provide numerical validation against real-world observations, we analyzed the differences between authentic and simulated SAR data using three numerical metrics: PSNR, MSE, and SSIM. These metrics helped establish the critical role of surface parameters in the accuracy of the SAR simulations. The evaluation consistently highlights that higher surface parameter values of surface parameters contribute to higher similarity scores for both building and ground surfaces. Notably, the reflection surface parameter lacks a distinct trend, implying a comparatively lesser impact on the visual appearance of simulated SAR imagery.

Furthermore, we explored the optimum LOD levels for a 3-D model through visual inspection and cross-sectional pixel profiles, our findings emphasize the efficacy of LOD3, particularly in recreating profiles within building scenarios. This highlights the importance of LOD3 in achieving high-fidelity simulations.

In the context of building damage assessment, our approach utilizing the EMS-98 scale with the 3-D models in SAR simulation yielded promising results. While SAR simulation effectively distinguishes damage classes at various resolutions,

challenges remain in discerning moderate damage at low resolution. However, the integration of collapsed walls damaged by tsunamis and earthquakes demonstrates the capability of SAR Simulations to represent diverse disaster scenarios.

Moreover, as we explore the potential of SAR simulations to assess damage severity, it becomes evident that continued research and refinement in simulation techniques are imperative for advancing the field. The feasibility of enhancing multiclass classification can be achieved by leveraging complementary data sources, such as generating SAR imagery from different angles, providing a more comprehensive understanding of damaged structural changes. Furthermore, exploring advanced machine learning techniques that integrate contextual information and domain-specific features holds promise for improving classification accuracy, especially in cases of moderate damage where visual cues are subtle.

In summary, our exploration significantly evaluates SAR simulation, providing pragmatic methodologies for refinement and augmenting the precision of 3-D model representations in diverse SAR applications. Looking ahead, our future work will explore alternative approaches for utilizing simulated SAR images, building upon the knowledge acquired to enhance realism and applicability across various applications, including machine learning data augmentation tasks. These findings bridge the gap between authentic and simulated SAR data, opening new possibilities for applications utilizing simulated SAR imagery.

REFERENCES

[1] B. Adriano, E. Mas, S. Koshimura, H. Gokon, W. Liu, and M. Matsuoka, "Developing a method for urban damage mapping using radar signatures of building footprint in SAR imagery: A case study after the 2013 super Typhoon Haiyan," in *Proc. IEEE Int. Geosci. Remote Sens. Symp.*, 2015, pp. 3579–3582.

[2] B. Adriano, S. Koshimura, S. Karimzadeh, M. Matsuoka, and M. Koch, "Damage mapping after the 2017 puebla earthquake in Mexico using high-resolution ALOS2 PALSAR2 data," in *Proc. IEEE Int. Geosci. Remote Sens. Symp.*, 2018, pp. 870–873.

[3] L. Giustarini et al., "Accounting for image uncertainty in SAR-based flood mapping," *Int. J. Appl. Earth Observ. Geoinf.*, vol. 34, pp. 70–77, 2015.

[4] J. Ruiz-Ramos, A. Marino, C. Boardman, and J. Suarez, "Continuous forest monitoring using cumulative sums of Sentinel-1 timeseries," *Remote Sens.*, vol. 12, no. 18, p. 3061, Sep. 2020.

[5] C.-U. Hyun, J.-H. Kim, H. Han, and H. Cheol Kim, "Mosaicking opportunistically acquired very high-resolution helicopter-borne images over drifting sea ice using COTS sensors," *Sensors*, vol. 19, no. 5, p. 1251, Mar. 2019.

[6] A. P. Nicolau, A. Flores-Anderson, R. Griffin, K. Herndon, and F. J. Meyer, "Assessing SAR c-band data to effectively distinguish modified land uses in a heavily disturbed amazon forest," *Int. J. Appl. Earth Observation Geoinf.*, vol. 94, 2021, Art. no. 102214.

[7] X. Ma, J. Xu, P. Wu, and P. Kong, "Oil spill detection based on deep convolutional neural networks using polarimetric scattering information from sentinel-1 SAR images," *IEEE Trans. Geosci. Remote Sens.*, vol. 60, 2022, Art. no. 4204713.

[8] R. Zhao, G.-H. Peng, W. Dong Yan, L.-L. Pan, and L.-Y. Wang, "Change detection in SAR images based on superpixel segmentation and image regression," *Earth Sci. Inform.*, vol. 14, no. 1, pp. 69–79, Nov. 2020.

[9] R. Dianat and S. Kasaei, "Change detection in optical remote sensing images using difference-based methods and spatial information," *IEEE Geosci. Remote Sens. Lett.*, vol. 7, no. 1, pp. 215–219, Jan. 2010.

[10] C. Ge, H. Ding, I. Molina, Y. He, and D. Peng, "Object-oriented change detection method based on spectral–spatial–saliency change information and fuzzy integral decision fusion for HR remote sensing images," *Remote Sens.*, vol. 14, no. 14, p. 3297, Jul. 2022.

[11] W. Liu, F. Yamazaki, H. Gokon, and S. Ichi Koshimura, "Extraction of tsunami-flooded areas and damaged buildings in the 2011 Tohoku-oki earthquake from TerraSAR-x intensity images," *Earthq. Spectra*, vol. 29, no. 1_suppl, pp. 183–200, Mar. 2013.

[12] F. Yamazaki, Y. Iwasaki, W. Liu, T. Nonaka, and T. Sasagawa, "Detection of damage to building side-walls in the 2011 Tohoku, Japan earthquake using high-resolution TerraSAR-X images," *Proc. SPIE*, vol. 8892, 2013, Art. no. 889212, doi: 10.1117/12.2029465.

[13] L. Gong, C. Wang, F. Wu, J. Zhang, H. Zhang, and Q. Li, "Earthquake-induced building damage detection with post-event sub-meter VHR TerraSAR-x staring spotlight imagery," *Remote Sens.*, vol. 8, no. 11, p. 887, Oct. 2016.

[14] N. Inkawhich et al., "Bridging a gap in SAR-ATR: Training on fully synthetic and testing on measured data," *IEEE J. Sel. Topics Appl. Earth Observ. Remote Sens.*, vol. 14, pp. 2942–2955, 2021.

[15] Q. Li, L. Gong, and J. Zhang, "A correlation change detection method integrating PCA and multi-texture features of SAR image for building damage detection," *Eur. J. Remote Sens.*, vol. 52, no. 1, pp. 435–447, Jan. 2019.

[16] K. Wu, G. Jin, X. Xiong, H. Zhang, and L. Wang, "SAR image simulation based on effective view and ray tracing," *Remote Sens.*, vol. 14, no. 22, p. 5754, Nov. 2022.

[17] S. Auer, R. Bamler, and P. Reinartz, "RaySAR - 3D SAR simulator: Now open source," in *Proc. IEEE Int. Geosci. Remote Sens. Symp.*, 2016, pp. 6730–6733.

[18] H. Hammer, T. Balz, E. Cadario, U. Soergel, U. Thoennessen, and U. Stilla, "Comparison of SAR simulation concepts for the analysis of high-resolution SAR data," in *Proc. 7th Eur. Conf. Synthetic Aperture Radar*, 2008, pp. 1–4.

[19] B. Lewis, T. Scarnati, E. Sudkamp, J. Nehrbass, S. Rosencrantz, and E. Zelnio, "A SAR dataset for ATR development: The synthetic and measured paired labeled experiment (SAMPLE)," *Proc. SPIE*, vol. 10987, 2019, Art. no. 109870H, doi: 10.1117/12.2523460.

[20] S. Kuny, H. Hammer, and K. Schulz, "Assessing the suitability of simulated SAR signatures of debris for the usage in damage detection," *Int. Arch. Photogrammetry Remote Sens. Spatial Inf. Sci.*, vol. XLI-B3, pp. 877–881, Jun. 2016.

[21] T. Balz, H. Hammer, and S. Auer, "Potentials and limitations of SAR image simulators a comparative study of three simulation approaches," *ISPRS J. Photogrammetry Remote Sens.*, vol. 101, pp. 102–109, Mar. 2015.

[22] Y. Sun, W. Jiang, J. Yang, and W. Li, "SAR target recognition using cGAN-based SAR-to-optical image translation," *Remote Sens.*, vol. 14, no. 8, p. 1793, Apr. 2022.

[23] S. Koshimura, L. Moya, E. Mas, and Y. Bai, "Tsunami damage detection with remote sensing: A review," *Geosciences*, vol. 10, no. 5, p. 177, May 2020.

[24] N. Y. D. Twumasi, Z. Shao, and O. Altan, "Remote sensing and GIS methods in urban disaster monitoring and management an overview," *Int. J. Trend Sci. Res. Develop.*, vol. 3, no. 4, pp. 918–926, Jun. 2019.

[25] B. Adriano et al., "Learning from multimodal and multitemporal earth observation data for building damage mapping," *ISPRS J. Photogrammetry Remote Sens.*, vol. 175, pp. 132–143, 2021.

[26] K. Molch, *"Radar earth observation imagery for urban area characterisation*," Joint Research Centre European Commission, Institute for the Protection and Security of the Citizen, Ispra, Italy, Rep., 2009.

[27] H. Hammer and K. Schulz, "Coherent simulation of SAR images," *Proc. SPIE*, vol. 7477, 2009, Art. no. 74771G, doi: 10.1117/12.830380.

[28] J. M. Allan and M. J. Collins, "SARSIM: A digital SAR signal simulation system," 2007. [Online]. Available: https://api.semanticscholar.org/CorpusID:16934147

[29] T. Balz and U. Stilla, "Hybrid GPU-based single- and double-bounce SAR simulation," *IEEE Trans. Geosci. Remote Sens.*, vol. 47, no. 10, pp. 3519–3529, Oct. 2009.

[30] C. Y. Ho, H. Neuschmidt, E. Mas, B. Adriano, and S. Koshimura, "Building damage estimation using RaySAR, a synthetic aperture radar simulator," 2023.

[31] S. Kuny, K. Schulz, and H. Hammer, "Signature analysis of destroyed buildings in simulated high resolution SAR data," in *Proc. IEEE Int. Geosci. Remote Sens. Symp.*, 2013, pp. 903–906.

[32] S. Kuny, H. Hammer, and K. Schulz, "Discriminating between the SAR signatures of debris and high vegetation," in *Proc. IEEE Int. Geosci. Remote Sens. Symp.*, 2015, pp. 473–476.

[33] J. Wang, J. Li, B. Sun, and Z. Zuo, "SAR image synthesis based on conditional generative adversarial networks," *J. Eng.*, vol. 2019, no. 21, pp. 8093–8097, Sep. 2019.

[34] S. I. Nikolenko, *Synthetic Data for Deep Learning*. Berlin, Germany: Springer, 2021.
[35] A. Jennison, B. Lewis, A. DeLuna, and J. Garrett, "Convolutional and generative pairing for SAR cross-target transfer learning," *Proc. SPIE*, vol. 11728, 2021, Art. no. 1172805, doi: 10.1117/12.2585898.
[36] G. F. Araujo, R. Machado, and M. I. Pettersson, "A tailored cGAN SAR synthetic data augmentation method for ATR application," in *Proc. IEEE Radar Conf.*, 2023, pp. 1–6.
[37] Z. Zuo and Y. Li, "A SAR-to-optical image translation method based on pix2pix," in *Proc. IEEE Int. Geosci. Remote Sens. Symp.*, 2021, pp. 3026–3029.
[38] S. Auer, T. Balz, S. Becker, and R. Bamler, "3D SAR simulation of urban areas based on detailed building models," *Photogrammetric Eng. Remote Sens.*, vol. 76, no. 12, pp. 1373–1384, Dec. 2010.
[39] S. Auer, S. Hinz, and R. Bamler, "Ray-tracing simulation techniques for understanding high-resolution SAR images," *IEEE Trans. Geosci. Remote Sens.*, vol. 48, no. 3, pp. 1445–1456, Mar. 2010.
[40] X. Bao, Z. Pan, L. Liu, and B. Lei, "SAR image simulation by generative adversarial networks," in *Proc. IEEE Int. Geosci. Remote Sens. Symp.*, 2019, pp. 9995–9998.
[41] Q.-Y. Zhou and U. Neumann, "2.5D dual contouring: A robust approach to creating building models from aerial LiDAR point clouds," in *Proc. Eur. Conf. Comput. Vis.*, 2010, pp. 115–128.
[42] S. Auer, *3D Synthetic Aperture Radar Simulation for Interpreting Complex Urban Reflection Scenarios*, 2011. [Online]. Available: https://books.google.co.jp/books?id=acaCnQEACAAJ
[43] M. Yang, P. Lopez-Dekker, P. Dheenathayalan, F. Biljecki, M. Liao, and R. F. Hanssen, "Linking persistent scatterers to the built environment using ray tracing on urban models," *IEEE Trans. Geosci. Remote Sens.*, vol. 57, no. 8, pp. 5764–5776, Aug. 2019.
[44] Y. Yu and W. Takeuchi, "Analysis of SAR backscatter intensity characteristics for inverse estimation of earthquake-damaged buildings," in *Proc. IEEE Int. Geosci. Remote Sens. Symp.*, 2022, pp. 350–353.
[45] A. Suppasri et al., "Damage characteristic and field survey of the 2011 great East Japan tsunami in Miyagi prefecture," *Coastal Eng. J.*, vol. 54, no. 1, pp. 1250005-1–1250005-30, Mar. 2012.
[46] IAEA, "IAEA expert team concludes mission to onagawa NPP," Aug. 2012. [Online]. Available: https://www.iaea.org/newscenter/pressreleases/iaea-expert-team-concludes-mission-onagawa-npp
[47] B. O. Community, "Blender—A 3D modelling and rendering package, blender foundation, stichting blender foundation," Amsterdam, 2018. [Online]. Available: http://www.blender.org
[48] Z. Wang, A. Bovik, and H. Sheikh, "Structural similarity based image quality assessment," in *Digital Video Image Quality and Perceptual Coding*. Boca Raton, FL, USA: CRC Press, Nov. 2005.
[49] A. Horé and D. Ziou, "Image quality metrics: PSNR vs. SSIM," in *Proc. 20th Int. Conf. Pattern Recognit.*, 2010, pp. 2366–2369.
[50] Z. Wang, A. Bovik, H. Sheikh, and E. Simoncelli, "Image quality assessment: From error visibility to structural similarity," *IEEE Trans. Image Process.*, vol. 13, no. 4, pp. 600–612, Apr. 2004.
[51] QGIS Development Team, "QGIS geographic information system, open source geospatial foundation," 2009. [Online]. Available: http://qgis.org
[52] F. Biljecki, H. Ledoux, and J. Stoter, "Redefining the level of detail for 3D models," *GIM Int.*, vol. 28, pp. 21–23, Nov. 2014.